Monthly Notices
of the
ROYAL ASTRONOMICAL SOCIETY

MNRAS **488,** 1489–1500 (2019)
Advance Access publication 2019 July 3

doi:10.1093/mnras/stz1740

The 'Red Radio Ring': ionized and molecular gas in a starburst/active galactic nucleus at $z \sim 2.55$

Kevin C. Harrington [1,2] A. Vishwas,[3] A. Weiß,[4] B. Magnelli,[1] L. Grassitelli,[1] M. Zajaček [4,5,6] E. F. Jiménez-Andrade [1,2] T. K. D. Leung,[3,7] F. Bertoldi,[1] E. Romano-Díaz,[1] D. T. Frayer,[8] P. Kamieneski,[9] D. Riechers,[3,10] G. J. Stacey,[3] M. S. Yun[9] and Q. D. Wang[9]

[1]*Argelander Institut für Astronomie, Auf dem Hügel 71, D-53121 Bonn, Germany*
[2]*International Max Planck Research School of Astronomy and Astrophysics, D-53121 Bonn, Germany*
[3]*Department of Astronomy, Cornell University, Space Sciences Building, Ithaca, NY 14853, USA*
[4]*Max-Planck-Institut für Radioastronomie (MPIfR), Auf dem Hügel 69, D-53121 Bonn, Germany*
[5]*Center for Theoretical Physics, Polish Academy of Sciences, Al. Lotnikow 32/46, PL-02-668 Warsaw, Poland*
[6]*I. Physikalisches Institut der Universität zu Köln, Zülpicher Strasse 77, D-50937 Köln, Germany*
[7]*Center for Computational Astrophysics, Flatiron Institute, 162 Fifth Avenue, New York, NY 10010, USA*
[8]*Green Bank Observatory, 155 Observatory Rd., Green Bank, WV 24944, USA*
[9]*Department of Astronomy, University of Massachusetts, 619E Lederle Grad Research Tower, 710 N. Pleasant Street, Amherst, MA 01003, USA*
[10]*Max-Planck-Institut für Astronomie, Königstuhl 17, D-69117 Heidelberg, Germany*

Accepted 2019 June 21. Received 2019 June 21; in original form 2019 March 15

ABSTRACT

We report the detection of the far-infrared (FIR) fine-structure line of singly ionized nitrogen, [N II] 205 μm, within the peak epoch of galaxy assembly, from a strongly lensed galaxy, hereafter 'The Red Radio Ring'; the *RRR*, at $z = 2.55$. We combine new observations of the ground-state and mid-J transitions of CO ($J_{\rm up} = 1$, 5, 8), and the FIR spectral energy distribution (SED), to explore the multiphase interstellar medium (ISM) properties of the *RRR*. All line profiles suggest that the H II regions, traced by [N II] 205 μm, and the (diffuse and dense) molecular gas, traced by CO, are cospatial when averaged over kpc-sized regions. Using its mid-IR-to-millimetre (mm) SED, we derive a non-negligible dust attenuation of the [N II] 205 μm line emission. Assuming a uniform dust screen approximation results a mean molecular gas column density $>10^{24}$ cm^{-2}, with a molecular gas-to-dust mass ratio of 100. It is clear that dust attenuation corrections should be accounted for when studying FIR fine-structure lines in such systems. The attenuation corrected ratio of $L_{\rm N\,II205}/L_{\rm IR(8–1000\,\mu m)} = 2.7 \times 10^{-4}$ is consistent with the dispersion of local and $z > 4$ SFGs. We find that the lower limit, [N II] 205 μm-based star formation rate (SFR) is less than the IR-derived SFR by a factor of 4. Finally, the dust SED, CO line SED, and $L_{\rm N\,II205}$ line-to-IR luminosity ratio of the *RRR* is consistent with a starburst-powered ISM.

Key words: gravitational lensing: strong – galaxies: evolution – galaxies: high-redshift – galaxies: ISM – galaxies: starburst.

1 INTRODUCTION

Observational evidence reveals a synchronous peak, around $z \sim 2$, in both the cosmic comoving star formation rate (SFR) and supermassive black hole accretion rate density (see e.g. Madau & Dickinson 2014; Hickox & Alexander 2018). Understanding this apparent co-evolution between active galactic nuclei (AGNs) and star formation (SF) demands a deeper characterization of the interstellar medium (ISM) in galaxies, such as the dynamics and spatial distribution of gas arising from different phases, as well as the relationship of ionized, molecular, and stellar surface mass densities and their role in SF processes. Substantial theoretical work (Dalla Vecchia & Schaye 2008; Scannapieco et al. 2012; Rosdahl et al. 2017) has also progressed in simulating the complex effects of black hole, thermal, and kinetic feedback processes, while observations of ISM properties derived from a broad-band coverage are still required to form a complete impression of a galaxy that has both

⋆ E-mail: kharring@astro.uni-bonn.de

an AGN and SF activity (Cicone et al. 2014, 2015, 2018). High-z star-forming galaxies (SFGs) at $z \sim 1$–3 typically show an increase in the molecular gas-to-stellar mass fractions (up to 50 per cent or greater; e.g. Tacconi et al. 2010, 2018). The spatial extent of SF within high-z SFGs can often exist out to large radii (∼2–10 kpc; e.g. Hailey-Dunsheath et al. 2010; Brisbin et al. 2015; Magdis et al. 2016; Elbaz et al. 2018), exceeding the 0.1–1 kpc nuclear starburst (SB) regions of local (Ultra)Luminous InfraRed Galaxies (LIRGs have $10^{10} < L_{\rm IR(8–1000\,\mu m)} < 10^{11}$ $L_\odot$ and ULIRGs have $L_{\rm IR(8–1000\,\mu m)} > 10^{12}$ $L_\odot$; Sanders & Mirabel 1996; Solomon et al. 1997; Solomon & Vanden Bout 2005a). Therefore global properties derived from measurements of the ionized and molecular ISM are needed to account for the total emission corresponding to the kpc-scale areas encompassed by high-z systems.

Studying the gas-rich, dusty star-forming galaxies (DSFGs) at $z > 1$ has largely focused on measurements of the molecular gas content via one or two CO lines (typically $J_{\rm up} \leq 5$), and also the long-wavelength dust continuum, to understand the star-forming ISM, the total molecular gas mass, and overall efficiency of SF (e.g. Genzel et al. 2010; Scoville et al. 2014; Schinnerer et al. 2016; Scoville et al. 2016, 2017; Harrington et al. 2018; Leung et al. 2019a; Dannerbauer 2019). The ionized ISM, however, has been largely unexplored at high-z, and therefore the complete picture of multiphase gas processes required to disentangle the nature of SF in galaxies are poorly constrained. Far-infrared (FIR) fine-structure lines (FSLs) offer an additional probe of H II regions in obscured sites of SF, as they are less susceptible to dust attenuation when compared to optical or mid-IR (MIR) lines (see Fernández-Ontiveros et al. 2016; Díaz-Santos et al. 2017). This motivates the use of these FIR FSLs as powerful line diagnostics of the evolving ISM at high-z (Maiolino et al. 2005, 2009; Ferkinhoff et al. 2010, 2011; Riechers et al. 2014; Lamarche et al. 2018; Marrone et al. 2018; Vishwas et al. 2018; Zanella et al. 2018; Zavala et al. 2018; Zhang et al. 2018). Unfortunately, the atmospheric coverage of many important mid-/far-IR FSLs makes observations difficult to execute, if not impossible to observe from the ground.

The nitrogen atom has an ionization energy $E_{i,N} = 14.53$ eV, and is therefore typically present with singly ionized hydrogen; $E_{i,H} = 13.6$ eV. The fine-structure splitting of the ground state leads to two transitions at 121.898 and 205.178 μm; [N II] 122 and [N II] 205 μm , respectively.[1] In order to characterize the global ionized ISM properties, the low-ionization energy requirement of the FIR [N II] emission lines makes them unique tracers of the low-excitation, warm ionized gas associated with H II regions and the ambient interstellar radiation field of the ISM. The physical and chemical evolution of the global ISM is influenced by supernova explosions and high mass-loss rates dispelled by stellar winds from massive OB and Wolf–Rayet type stars (e.g. McKee & Williams 1997; Crowther 2007; Puls, Vink & Najarro 2008). These, together with efficient rotational mixing within massive stars (Maeder & Meynet 2000; Brott et al. 2011; Ekström et al. 2012), can quickly expose the products of stellar nucleosynthesis at the surface, thereby injecting substantial quantities of nitrogen into the ISM within a time-scale of ∼10 s Myr (Maeder & Meynet 2000; Stanway & Eldridge 2019).

The [N II] emission lines were first observed in the Milky Way by the COBE FIRAS spectrometre (Bennett et al. 1994), followed closely by KAO observations of the Galactic H II region G333.6-0.2 (Colgan et al. 1993). The [N II] 205 μm line is also observable at rest velocities from the ground-based observatories at exceptional sites. Using the SPIFI spectrometer on the AST/RO telescope at South Pole, Oberst et al. (2006, 2011) mapped the [N II] 205 μm line from the Carina Nebula and compared it with ISO LWS [N II] 122 μm line maps to show the [N II] line originated from a low-density ($n_{e^-} \sim 28$ cm^{-3}) ionized medium. High spatial resolution, large-scale imaging of the Galactic plane were enabled by the sensitive PACS and SPIRE spectrometer onboard the *Herschel Space Observatory* (Goldsmith et al. 2015), and demonstrated that most of the [N II] line arises from extended, low-density ($n_{e^-} \sim 10$ to 50 cm^{-3}) H II regions. Other efforts to use [N II] to derive average electron densities have been made in a range of local galaxies ($n_{e^-} \sim 20$–100 cm^{-3}), for instance: M51 and Centaurs A, (Parkin et al. 2013), ULIRGs (HERUS sample; Farrah et al. 2013), Dwarf galaxies (Cormier et al. 2015), KINGFISH galaxies (Herrera-Camus et al. 2016), and other SFGs (Lu et al. 2017).

At high-z, observations of the [N II] 205 μm line is largely limited to $z > 3.9$, where the line is redshifted to wavelengths longer than 1mm, making ground-based observations possible due to the more transmissive and stable atmosphere, with lower receiver noise temperatures. The current sample where this emission line is detected consists of at least thirteen highly SFGs (Combes et al. 2012; Decarli et al. 2012, 2014; Nagao et al. 2012; Rawle et al. 2014; Béthermin et al. 2016; Pavesi et al. 2016, 2018a,b; Lu et al. 2018; Tadaki 2019), and there are at least five additional non-detections (see Walter et al. 2009; Riechers et al. 2013).

In this paper we report new spatially unresolved line detections from 'The Red Radio Ring' (hereafter: the *RRR*) of [N II] 205 μm line emission with the APEX telescope, complemented by CO(1–0), CO(5–4), and CO(8–7) line detections from the *Green Bank Telescope* (GBT) and IRAM 30 m telescope. The [N II] 205 μm line detection at the redshift, $z \sim 2.55$, in the *RRR* begins to bridge the gap between local detections and those at $z > 4$.

We structure the paper as follows, in Section 2 we provide a brief outline of the nature of the galaxy presented in this study. We describe the [N II] and CO observations in Section 3, and then present the results in Section 4. In Section 5 we discuss the [N II] derived SFR and the possibility for a co-eval AGN/SB, followed by our conclusions and outlook in Section 6. Throughout this paper we take for a point of reference a flat ΛCDM cosmology with $H_0 = 69.6$ km s^{-1} Mpc^{-1} with $\Omega_m = 0.286$, and $\Omega_\Lambda = 1 - \Omega_m$ (Bennett et al. 2014). Throughout the text, we use a magnification factor, $\mu = 15$, to report the intrinsic source properties unless otherwise noted. This value is derived from lens models using the highest spatial resolution data available for this source, i.e. $\mu = 14.7 \pm 0.3$, (Geach et al. 2018), and is consistent with other work (Rivera et al. 2018; Kamieneski et al., in preparation). The relative magnification factor, however, can change depending on the source plane distribution of every line and continuum tracer at varying rest frequencies.

2 THE RED RADIO RING

The *RRR* was discovered by four independent teams: (i) the citizen science program *SpaceWarps* (Marshall et al. 2016) in a search for gravitational lensing features within deep (iJKs band) CFHT images in the *Herschel*-Stripe82 field (Geach et al. 2015); (ii) Harrington et al. (2016) identified this source after cross-matching *Herschel*-SPIRE and *Planck* images at 350 μm in order to identify strongly

[1]The ground state ($^3P_0$) fine-structure splitting arises due to the unpaired electrons in the nitrogen atom. The $^3P_2$ and $^3P_1$ levels are only about 188 and 70 K above ground, respectively.

lensed DSFGs (Negrello et al. 2010; Fu et al. 2012; Wardlow et al. 2013; Cañameras et al. 2015; Planck Collaboration XXVII 2015) and further confirmed with follow-up CO and millimetre dust continuum observations with the *Large Millimeter Telescope*; (iii) Nayyeri et al. (2016) present a similar selection of candidate lensed DSFGs as Harrington et al. (2016), but with SPIRE 500 μm images instead; and (iv) Su et al. (2017) identified the *RRR* as the brightest DSFG candidate (referred to as ACTJ0210+0016) in the 148, 218, and 278 GHz maps from the *Atacama Cosmology Telescope* (*ACT*), and presented follow-up CO(1–0) line observations with *Green Bank Telescope*/Zpectrometer.

The *RRR* is a strongly lensed radio-AGN/DSFG hybrid galaxy, magnified by a massive, foreground elliptical galaxy and a satellite companion at $z = 0.2019$ (Geach et al. 2015). The 1.4 GHz eMERLIN imaging ($\theta \sim 0.35$ arcsec) revealed compact radio emission <250 pc in the lens reconstructed source-plane image. The intrinsic specific radio luminosity $L_{1.4\mathrm{GHz}} \approx 10^{25}\,\mathrm{W\,Hz^{-1}}$ suggests a radio-mode AGN (Geach et al. 2015). The wavelength corresponding to the peak line flux of the asymmetric low-J CO line profile corresponds to a redshift, $z \sim 2.553$ for the *RRR* (Harrington et al. 2016; Su et al. 2017). Detailed strong lens modelling of the CO(3–2) emission resolved by NOEMA ($\theta \sim 0.75 \times 1.5$ arcsec) suggests that the observed molecular gas emission arises from a rotating disc spread over ∼3 kpc in the source plane (Rivera et al. 2018). The source-plane reconstruction of the CO(4–3) line emission ($\theta \sim 0.25$ arcsec) by Geach et al. (2018) provides evidence that the growth of the AGNs is co-eval with the rapid SF. The molecular gas may dominate the galactic potential within these 3 kpc, which is further supported by Rivera et al. (2018).

3 OBSERVATIONS

3.1 GBT

The CO(1–0) line emission was observed using the Ka-band receiver on the GBT. Observations (GBT/17B-305; PI: K. Harrington) took place on 2017 October 22, under stable atmospheric conditions. We used the standard SubBeamNod procedure between the 8 m subreflector and the main dish, with 4 min integrations per scan. Pointing and focus were performed frequently before the SubBeamNod integrations. The backend spectrometer, VEGAS, was used to record the data from the Ka-band receiver, tuned to the expected CO(1–0) line frequency (in low-resolution 1.5 GHz bandwidth mode; $\theta \sim 23$ arcsec). Subsequent data reduction was performed using GBTIDL (Marganian et al. 2013). All on–off measurements were corrected for the atmospheric attenuation and afterwards treated in the same manner as in Harrington et al. (2018). We smoothed all spectra to 50 $\mathrm{km\,s^{-1}}$ channel resolution after averaging all low-order baseline subtracted spectra. The resulting on-source integration time was 1.25 h. Flux accuracy was checked with the standard source Uranus and pointing stability with J0841+7053, J1310+3220, J1331+3030, and J1642 + 3948. We adopt a 25 per cent uncertainty on the integrated line properties for systematic effects with the GBT (see Frayer et al. 2018; Harrington et al. 2018).

3.2 APEX

To observe the [N II] 205 μm emission line we used the FLASH$^+$460L single polarization receiver on the Atacama Pathfinder EXperiment (APEX) 12 m telescope (Güsten et al. 2006). We used Max Planck Society observing time between 2018 24 May and 17 July (Pr. M-0101.F-9503A-2018; PI: Harrington), totalling 384 min of integration ($\theta \sim 15$ arcsec). FLASH (Heyminck et al. 2006) is a 2 sideband (SB) dual-frequency heterodyne receiver with orthogonal linear polarizations, one for each of the 345 and 460 GHz atmospheric windows. The FLASH observations were performed in good weather conditions, with precipitable water vapour <1.5 mm. Observations used standard wobbler switching with a chopping rate of 1.5 Hz, and an azimuthal throw offset of 30 arcsec. Each scan consisted of a hot/sky/cold calibration 600 arcsec off-source, followed by 12 subscans of 20 s per on-source integration time. Focus checks were performed regularly (every 3–5 h), whereas pointing checks on a strong line/continuum source (e.g. Jupiter or nearby star) were performed roughly every 1–2 h and yield a pointing accuracy within 2–3 arcsec. To record the data we used the MPIfR eXtended bandwidth Fast Fourier Transform spectrometers (FFTS; Klein et al. 2006) with a 2 × 2.5 GHz bandwidth for each of the upper and lower receiver sidebands of spectra the FLASH receiver. All scans were reduced and analysed using the CLASS and GREG packages within the *gildas*[2] software distribution. Each scan was smoothed to ∼90 $\mathrm{km\ s^{-1}}$ channel resolution and assessed by eye after a first order baseline polynomial subtraction (line-free channels). Only about 10 per cent of the scans were removed for each set of spectra before co-adding the rms-weighted spectrum. We adopt an absolute uncertainty of 25 per cent for all derived line properties to account for the variations in systematic behaviour of the APEX observations at higher frequencies (e.g. atmospheric stability, baseline subtraction, pointing/focus corrections).

3.3 IRAM 30 m

Observations with the IRAM 30 m telescope took place across two observing semesters: Pr. 187-16 and Pr. 170-17 (PI: K. Harrington), starting on 2017 January 29th we observed the CO(5–4) emission line in average weather conditions ($\tau_{\nu\mathrm{obs}} = 0.5$–$0.8$) for 30 min of integration. Subsequent observations were in excellent observing conditions ($\tau_{\nu\mathrm{obs}} < 0.04$–$0.2$) on 2017 December 13 for roughly 35 min integration to detect the CO(8–7) emission line. We used the E150 and E230 observing bands of the EMIR receiver, and utilized two backends: both the WIde-band Line Multiple Autocorrelator (WILMA) and the FFTS (FTS200). Our observing mode consisted of a single EMIR band, capturing the dual polarization, 16 GHz bandwidth of the lower inner and lower outer (LI+LO), and upper inner and upper outer (UI + UO) sidebands with respect to the LO tuning frequency. To overcome the variable atmospheric conditions, we used the wobbler switching observing mode to perform offset throws of 40 arcsec every second. Each wobbler switching mode procedure includes three 5 min integrations (i.e. twelve 25 s subscans). Frequent focus and pointing checks were assessed (e.g. Uranus, Venus, J1226+023, J1418+546) every 1.5–2 h, with azimuth and elevation pointing offsets typically within 3 arcsec. The IRAM 30 m beam sizes at the observed CO(5–4) and CO(8–7) line frequency are $\theta \sim 15$ and $\theta \sim 10$ arcsec, respectively. The absolute uncertainty we adopt for the derived line properties from the IRAM 30 m observations is 20 per cent based on the dispersion of flux densities observed in pointing sources from ongoing monitoring at the telescope. All scans were reduced using GILDAS, smoothed to ∼50 $\mathrm{km\ s^{-1}}$ channel resolution before being co-added.

[2]Software information can be found at: http://www.iram.fr/IRAMFR/GILDAS.

Table 1. Best-fitting Gaussian models and line properties.

	[N II]205 μm	CO(1–0)	CO(3–2)[a]	CO(4–3)[c]	CO(5–4)	CO(8–7)
Redshift, z (peak)	2.55308 (0.0004)	2.55300 (0.0004)	2.5529 (0.00011)	2.5543 (0.0002)	2.5525 (0.0002)	2.55243 (0.0003)
			Total intrinsic line properties[b]:			
$S_v\Delta V$ (Jy km s^{-1})	4.3 (1.1)	0.18 (0.04)	1.38 (0.28)	1.62 (0.32)	1.96 (0.3)	1.37 (0.27)
L' (10^{10} K km s^{-1} pc^2)	0.84 (0.21)	3.67 (0.92)	4.8 (1.2)	3.2 (0.8)	2.5 (0.6)	0.67 (0.19)
$L_{\rm line}$ (10^8 L$_\odot$)	8.4 (2.0)	0.02 (4.3e-03)	0.64 (0.02)	1.0 (0.25)	1.5 (0.38)	1.6 (0.42)
			Component A (peak):			
FWHM (km s^{-1})	293 (76)	179 (23)	–	–	165 (22)	154 (50)
Amplitude (mJy)	8.7 (1.3)	0.44 (0.07)	–	–	5.5 (0.7)	5.1 (2.0)
Centre (km s^{-1})	−69 (34)	−55 (10)	–	–	−37 (6)	−20 (17)
			Component B:			
FWHM (km s^{-1})	337 (170)	352 (230)	–	–	480 (116)	337 (353)
Amplitude (mJy)	4.5 (1.3)	0.09 (0.023)	–	–	2.10 (0.25)	1.5 (0.6)
Centre (km s^{-1})	334 (72)	200 (118)	–	–	240 (60)	200 (188)

The velocities are measured with respect to $z = 2.553$, i.e. the peak velocity component.
[a]Su et al. (2017) and Rivera et al. (2018) corrected for the cosmology used throughout this paper.
[b]Measured line properties corrected for magnification ($\mu = 15$). The systematic errors are listed in parenthesis for the velocity-integrated flux density and derived total line luminosities. The parenthesis associated with the FWHM, centroid, and amplitude for Gaussian components A and B are based on the residual errors to the model fit.
[c]Geach et al. (2018) corrected for the cosmology used throughout this paper. Geach et al. (2018) report the redshift based on the mid-point full-width-at-zero-intensity of the observed CO(4–3) transition.

4 RESULTS

4.1 Intrinsic line properties

The observed [N II] 205 μm emission line peaks at $\nu_{\rm obs}^{\rm peak} = 411.2485$ GHz. We integrate the full line profile to derive a total velocity integrated flux density of 4.3 ± 1.1 Jy km s^{-1} (using an antenna gain factor of 52.3 Jy K^{-1}). The CO(1–0) ($\nu_{\rm obs}^{\rm peak} = 32.4432 \pm 0.0001$ GHz) has a measured integrated flux of 0.18 ± 0.04 Jy km s^{-1} (antenna gain factor of 0.7 Jy K^{-1}). This is consistent with, albeit slightly higher than, the Zpectrometer measurement (0.11 ± 0.03 Jy km s^{-1}) of Su et al. (2017). The velocity integrated flux intensities for the CO(5–4) ($\nu_{\rm obs}^{\rm peak} = 162.212$ GHz) and CO(8–7) ($\nu_{\rm obs}^{\rm peak} = 259.484$ GHz) emission lines are 1.96 ± 0.3 and 1.37 ± 0.27 Jy km s^{-1}, using antenna gain factors of 6.69 and 8.38 Jy K^{-1}, respectively. We report in Table 1 the line luminosity (in L$_\odot$) and spatially integrated source brightness temperature (in K km s^{-1} pc^2) following Carilli & Walter (2013). We note that the peak line intensity frequencies are all consistent with $z = 2.5535 \pm 0.0006$.

Asymmetric line profiles are observed in all the high-S/N ($S_{\rm peak}/N_{\rm rms} > 10$) line detections (CO 1–0, 5–4, 8–7; [N II] 205 μm), therefore we fit two 1D Gaussians to the line shapes to compare their respective full width at half-maximum (FWHM), centroids, and amplitudes. The best-fitting models are overlaid on the CO and [N II] 205 μm spectra in Fig. 1, while the best-fitting parameters are listed in Table 1, together with the CO(3–2)[3] and CO(4–3) velocity integrated line flux densities from Rivera et al. (2018) and Geach et al. (2018).

The line centroid and FWHM of the [N II] 205 μm emission line are consistent with the observed CO(1–0) (tracing the total molecular gas mass), and the more highly excited, $J_{\rm up} > 3$, CO lines. In all lines, the red component is offset by about 250–450 km s^{-1} from the blue component. Differential lensing may yield differences in measured line ratios (Serjeant 2012). However, without higher angular resolution observations for each transition, we assume the magnification factor does not change for each of the observed lines, such that the low-density diffuse H II regions traced by [N II] 205 μm and the molecular gas traced by CO are considered to be cospatial when averaged across kpc scales.

[3]As noted in Rivera et al. (2018), the CO(3–2) line flux for the LMT detection presented in Harrington et al. (2016) is unfortunately incorrect due to the early commissioning period and calibration uncertainties.

4.2 FIR spectral energy distribution

Using data from the literature and various telescope archives, we compiled multiband photometry tracing emission from the *RRR* in the (observed-frame) MIR to mm-wavelengths (Geach et al. 2015; Harrington et al. 2016; Schulz et al. 2017; Su et al. 2017). We fit the observed spectral energy distribution (SED) with a single-temperature modified blackbody (MBB) model combined with a Wien-side power-law slope, denoted as α, of which a value of $\alpha \sim 2$ is characteristic for SFGs (e.g. Casey et al. 2012). If an AGN torus is contributing a hot dust component, the MIR would show an excess compared to the power-law slope for a normal SFG (e.g. the WISE 'Hot DOGS', Tsai et al. 2015).

We retrieved the SPIRE photometer measurements from the SPIRE point source catalogue (Schulz et al. 2017). We report the estimated uncertainties due to confusion rather than the systematic and statistical errors (which are <2 per cent) as the SPIRE beam is large (18–35 arcsec) and the diameter of the radio Einstein ring is roughly 5 arcsec (Geach et al. 2015). We find that the flux density measured with LMT/AzTEC varies by 50 per cent between the two observations by Geach et al. (2015) and Harrington et al. (2016, see footnote 3 above). For the MBB fit, we use the average value of these measurements, with an uncertainty that encompasses the range of values reported, i.e. 125 ± 35 mJy. We note that Geach et al. (2015) reported that the 450μm flux density measured with SCUBA was a factor of 3 smaller than that measured by SPIRE and hence this SCUBA measurement not included here. In comparison with the ACT 278 GHz measurement, we find that the 850 μm SCUBA flux density, though a high significance detection, is most likely an underestimate, perhaps due to absolute flux calibration. We therefore ignore the SCUBA 850 μm data point while performing the model fitting.

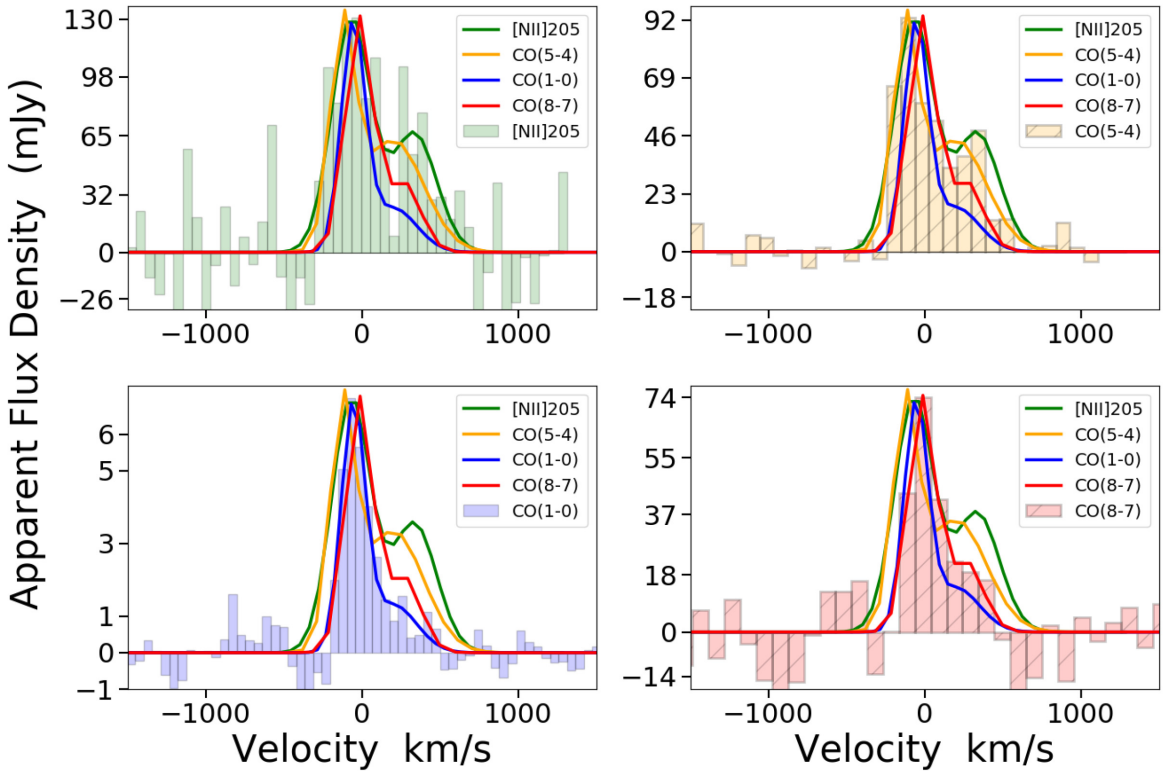

Figure 1. The spectra and two-component Gaussian fits for the [N II] 205 μm (green; top left), CO(1–0) (blue; bottom left), CO(5–4) (orange; top right), and CO(8–7) (red; bottom right) lines. To aid comparisons among all line profiles, the best-fitting Gaussian models have been rescaled to the observed peak of each spectrum within each panel. The zero-point velocity is determined using $z = 2.553$.

Fig. 2 shows the best-fitting SED model of the *RRR*. In the following we quote the best fitting and the uncertainties based on the 16th, 50th, and 84th percentiles of the samples in the marginalized distributions for each of the parameters (see Fig. 3). We find the dust opacity reaches unity at rest-frame wavelength of $\lambda_0 = 254^{+17}_{-18}$ μm, with a dust emissivity index $\beta = 2.0^{+0.17}_{-0.17}$, and a dust temperature, $T_d = 55^{+2.3}_{-2.2}$ K, Wien-side power-law slope $\alpha = 2.27^{+0.14}_{-0.11}$. The total *apparent* IR luminosity (8–1000μm), $\mu L_{IR} = 21.9^{+1.0}_{-0.89} \times 10^{13}\,L_\odot$, before correcting for the magnification factor, μ. The *apparent* FIR luminosity (40–120μm), is $\mu L_{FIR} = 12.3^{+0.41}_{-0.43} \times 10^{13}\,L_\odot$. The value of L_{IR}/L_{FIR} is consistent with normal star-forming systems, i.e. $L_{IR}/L_{FIR} \approx 1.5$–2 (Dale et al. 2001; see e.g. Leung et al. 2019b). Thus, the observed dust SED does not show strong signs of an AGN influence, e.g. no bright WISE/W4 counterpart. This suggests (i) that the compact radio-AGN, revealed by bright radio emission with a steep radio synchrotron slope of $\alpha_{radio} = -1.1$ (Geach et al. 2015), does not significantly affect the overall IR luminosity of the *RRR*, or (ii) there is extreme dust obscuration of an AGN. Its intrinsic SFR can thus be estimated using $\mu = 15$ (Geach et al. 2018) and the standard calibration of the total IR to SFR, with ($SFR_{IR} = 1.7 \times 10^{-10} L_{IR}\ M_\odot\ yr^{-1}$; Kennicutt 1998). We find the $SFR_{IR} = 2482 \pm 992\,M_\odot\,yr^{-1}$, taking into account the total error propagation for the average best-fitting relative uncertainty on the IR luminosity (∼3 per cent), and the systematic errors for the photometric data points used in the modelling (∼37 per cent; Table 2).

4.2.1 *Effects of dust attenuation*

In the *RRR* the dust opacity reaches unity at the rest-frame wavelength of $\lambda_0 = 254$ μm. Such high opacity is consistent with that observed in other high-z DSFGs (Riechers et al. 2013), while slightly higher than e.g. AzTEC-3, which is a more normal SFG at $z > 5$, (Riechers et al. 2014). The dust attenuation of the [N II] 205 μm emission line is therefore not negligible, as pointed out by other studies of FIR FSLs in quasars (QSOs) and DSFGs (Uzgil et al. 2016; Lamarche et al. 2017, 2018). We correct the line luminosity based on a single, uniform dust screen approximation, i.e. $L_{[N\,II]205_{un-att.}} = e^{\tau_{205\,\mu m}} \times L_{[N\,II]205,obs.}$. From our best-fitting SED model, the opacity at rest-frame 205 μm is $\tau_{205\,\mu m} = (\lambda_0/\lambda)^\beta = 1.54$, which results in a uniform screen dust attenuation correction factor of $e^{\tau_{205\,\mu m}} \simeq 4.67$. The following corrections are considered an upper limit along the line of sight. In the scenario where the emitting gas is well mixed with dust, the mixed gas/dust attenuation correction factor would be $\tau_{205\,\mu m}/(1 - e^{-\tau_{205\,\mu m}}) = 1.96$.

Corrections to the observed FIR FSL detections of the $z > 4$ systems are limited by the sparse sampling of their peak dust SED to accurately constrain the dust opacity at the relevant wavelength. The *RRR*, with its well-sampled dust SED, allows us to constrain the mean hydrogen column density N_{H_2}. In the following analysis, we assume both a fixed gas-to-dust-mass ratio, GDMR = 100, and a simple uniform dust screen. The dust opacity is expressed in terms of the dust column density, N_d, and κ_ν, the mass absorption coefficient (Weiß et al. 2008). We express N_d as N_{H_2} multiplied by the mass of molecular hydrogen, m_{H_2}, divided by the GDMR:

$$\tau_\nu = \kappa_\nu \times N_d = \kappa_\nu \times \frac{N_{H_2} \times m_{H_2}}{GDMR}, \quad (1)$$

where

$$\kappa_\nu = 0.04\,(\nu/250GHz)^\beta. \quad (2)$$

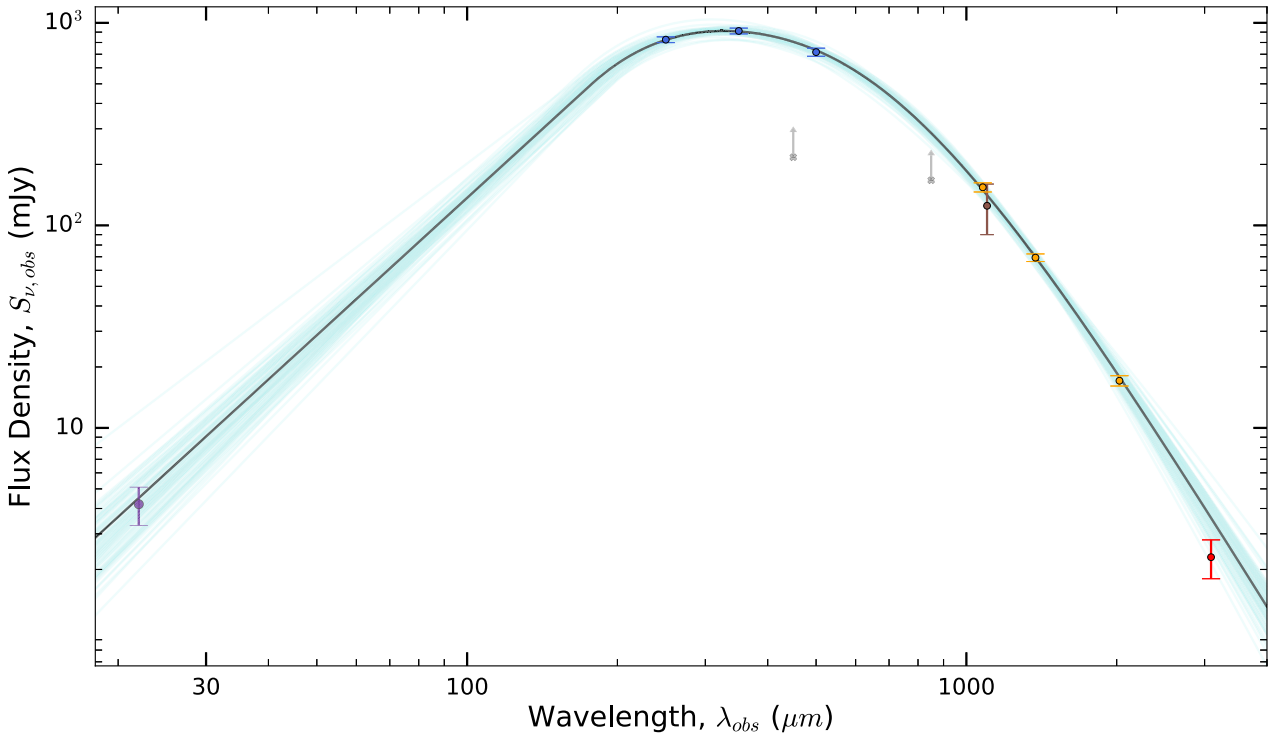

Figure 2. The best-fitting MBB SED model (black line) for the *RRR*. We also show multiple iterations of the models created by sampling the parameter space for the MBB (cyan) that are representative of the degeneracies in the parameter space. Data included for the SED fit exercise is shown as coloured circles with corresponding error bars: (indigo) *WISE*/W4, (blue) *Herschel*/SPIRE, (yellow) ACT (Su et al. 2017), and (red) CARMA (Su et al. 2017). For completeness, we show data that is not included for the SED fit - (grey cross as lower limits) measurements from SCUBA-2 presented in Geach et al. (2015) and (brown circle) is the average of the two AzTEC/LMT measurements from Geach et al. (2015) and Harrington et al. (2016).

Fig. 4 plots the dust attenuation correction as a function of the mean molecular hydrogen column density N_{H_2} at rest-frame wavelengths corresponding to the [N II] 205, [N II] 122, and [C II]158 μm emission lines. The equivalent H_2 gas column density in the *RRR* is $N_{H_2} = 3.3 \times 10^{24}$ cm^{-2}.

The *RRR*, having high molecular gas column densities, will have corrections that can severely impact the use of both [N II] 205 and [N II] 122 μm emission lines as an electron density indicator. For example, based on this simple uniform screen approximation, the observed line ratio of [N II] 122 μm / [N II] 205 μm in the *RRR* would need to be corrected by a factor of $e^{\tau_{122\,\mu m}}/e^{\tau_{205\,\mu m}} \approx 18$. An intrinsic [N II] 122 μm / [N II] 205 μm line ratio of ∼4–5, corresponding to an electron density of $n_{e^-} \simeq 200\,\mathrm{cm}^{-3}$ (e.g. in the local starburst, M82; Petuchowski et al. 1994), would thus yield an observed [N II] 122 μm / [N II] 205 μm value of (4–5)/18 = 0.3. Neglecting dust opacity, one would associate such low observed line ratio to unphysically low densities, as it would lie below the minimum theoretical line ratio of ≈0.6, as derived for warm ionized regions with $n_{e^-} << n_{\mathrm{crit},205\,\mu m}$ (Goldsmith et al. 2015; Herrera-Camus et al. 2016). Naturally, the *RRR*, but also all high-z systems resembling the *RRR*, i.e. having high column densities, would suffer from this effect. Dust opacity should not be neglected while studying FIR FSL emission in high-z DSFGs.

4.2.2 *Relative cooling by [N II] 205 μm line luminosity*

Using the [N II] 205 μm and IR luminosities, we calculate the attenuation corrected $L_{[\mathrm{N\,II}]205\,\mu m}/L_{\mathrm{IR}} = 2.7 \pm 1.0 \times 10^{-4}$, assuming the same magnification factor for both luminosities. The vast majority of the local and high-z galaxies do not correct for dust attenuation, therefore we use the apparent, attenuated value, $L_{[\mathrm{N\,II}]205\,\mu m}/L_{\mathrm{IR}} = 5.8 \pm 2.1 \times 10^{-5}$.

As seen in Fig. 5, this attenuated $L_{[\mathrm{N\,II}]205\,\mu m}/L_{\mathrm{IR}}$ ratio for the *RRR* is at the lower boundary of the mean range observed in local ULIRGs within the large scatter of $10^{-5} - 10^{-3}$ (Zhao et al. 2016). The large dispersion in the $L_{[\mathrm{N\,II}]205\,\mu m}/L_{\mathrm{IR}}$ ratio remains constant across all redshifts. Galaxies in Fig. 5 with the lowest values of $L_{[\mathrm{N\,II}]205\,\mu m}/L_{\mathrm{IR}}$ include strong QSOs at $z \sim 4$ (e.g. Decarli et al. 2012), as well as the local AGN, MrK231, which has at least a 20 per cent AGN fraction contributing to its $L_{\mathrm{IR}} \approx 10^{12}$ L$_\odot$ (Fischer et al. 2010; Dietrich et al. 2018). SFGs at high-z have slightly large scatter, probing a range of up to a factor of 5 between low-metallicity galaxies (Pavesi et al. 2018b), DSFGs, and a Lyman-α Emitter (Decarli et al. 2014).

The $L_{[\mathrm{N\,II}]205\,\mu m}/L_{\mathrm{IR}}$ ratio of the *RRR* more closely resembles that of local/high-z SB rather than that of local/high-z QSO/AGNs. To first order, the global ISM within the *RRR* is mostly powered by SF. We note, however, that this ratio is subject to a few caveats. Robust comparisons of this ratio between the *RRR* and to other systems can be affected by individual variations in attenuation effects and hard ionizing radiation fields that determine the relative [N II] 205 μm line emission. The bolometric input to the total IR luminosity from a supermassive black hole accretion/activity could contaminate the apparent IR luminosities and reduce the observed line to total FIR luminosity, as seen in QSO-selected systems. However, this ratio may not decrease significantly if there is a narrow emission line region of an AGN contributing to the total [N II] 205 μm line luminosity, as seen in the local selection of AGN via the [N II] 6584 Å / 6548 Å excess (Baldwin, Phillips & Terlevich 1981). Our dust

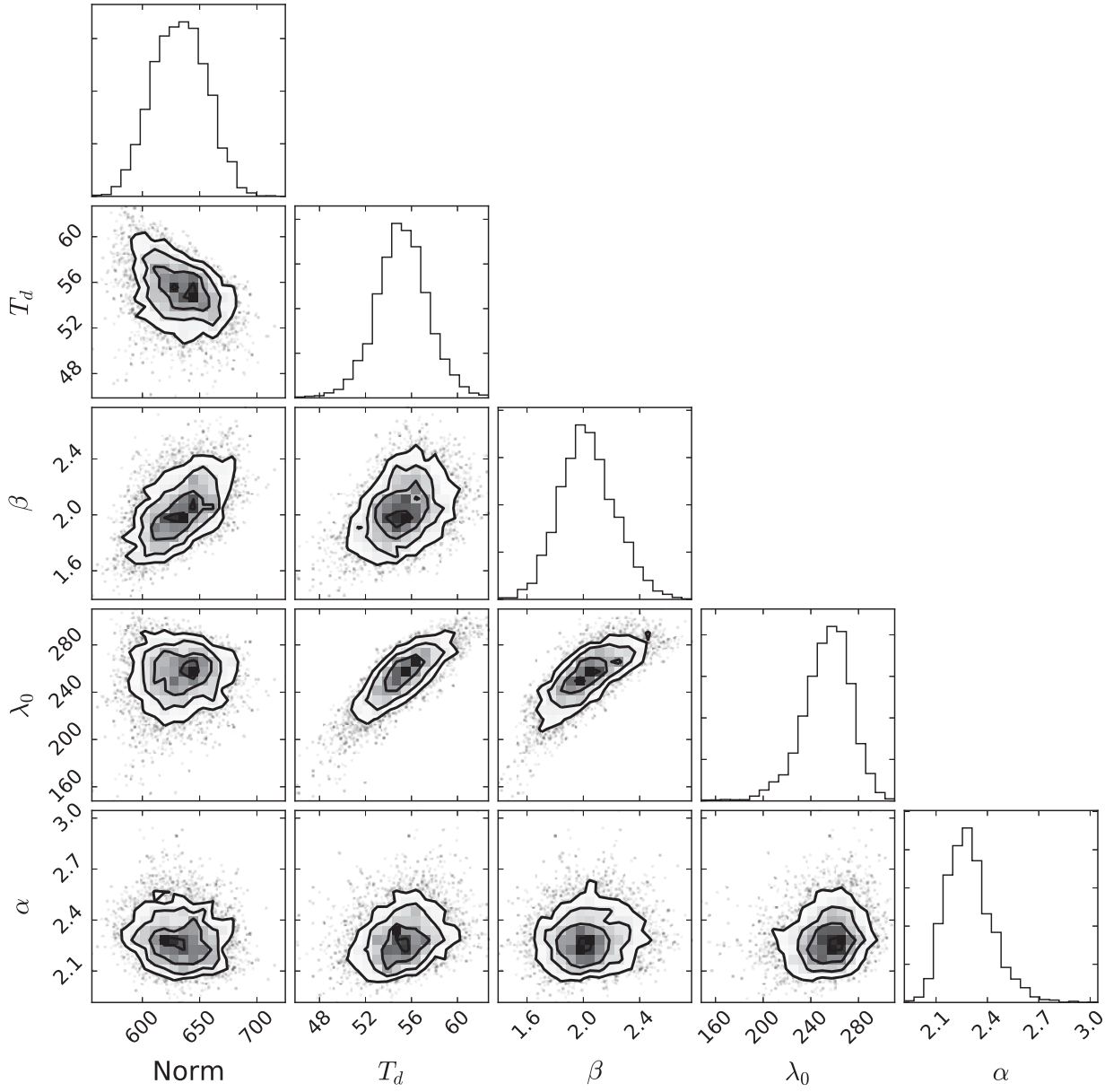

Figure 3. Posterior probability distribution for the SED model parameters: the value at which the dust opacity reaches unity is at rest-frame wavelength of λ_0, dust emissivity index, β, a single component dust temperature, $T_{\rm d}$, and the Wien-side power-law slope for SFGs, α.

Table 2. Observed MIR to mm photometry for the *RRR*.

Wavelength (μm)	Flux density (mJy)	Instrument
22	4.2 ± 0.9	*WISE*/W4
250	880 ± 27	*Herschel*/SPIRE
350	991 ± 30	*Herschel*/SPIRE
500	773 ± 33	*Herschel*/SPIRE
850	167 ± 4	JCMT/SCUBA (G15)
1078.4	154 ± 8	ACT (278GHz, S17)
1100	95.5 ± 6	LMT/AzTEC (G15)
1100	145 ± 15	LMT/AzTEC (H16)
1375.2	69 ± 3	ACT (218GHz, S17)
2025.6	17 ± 2	ACT (148GHz, S17)
3090.6	2.3 ± 0.5	CARMA (S17)

Geach et al. (2015, G15), Harrington et al. (2016, H16), and Su et al. (2017, S17).

SED model is consistent with that of an SB galaxy (Casey et al. 2012; Magnelli et al. 2014), yet the resemblance of such an SED can also be due to a large dust screen strongly attenuating the emission from an obscured, dusty AGN torus ($T_{\rm d} \approx 500$ K; Siebenmorgen, Krügel & Spoon 2004; Siebenmorgen, Heymann & Efstathiou 2015; Feltre et al. 2012; Kirkpatrick et al. 2017; Leung et al. 2019b). Thus, the spatially unresolved measurement of $L_{[\rm N\,II]205\,\mu m}/L_{\rm IR}$ ratio cannot exclusively select an AGN from an SFG.

In our local Universe, the observed scatter correlates with the rest-frame log $(f_{70\,\mu m}/f_{160\,\mu m})$ colour (Zhao et al. 2013, 2016). SFGs with colder colours have an average of $L_{[\rm N\,II]205\,\mu m}/L_{\rm IR} \sim 3 \times 10^{-4}$, while star-forming/SB galaxies with warmer colours have average values of the $L_{[\rm N\,II]205\,\mu m}/L_{\rm IR}$ ratio of $\sim 5 \times 10^{-5}$ (Zhao et al. 2016). We show in Fig. 5 the range observed in the local Universe within galaxies with a similar FIR colour as the *RRR*

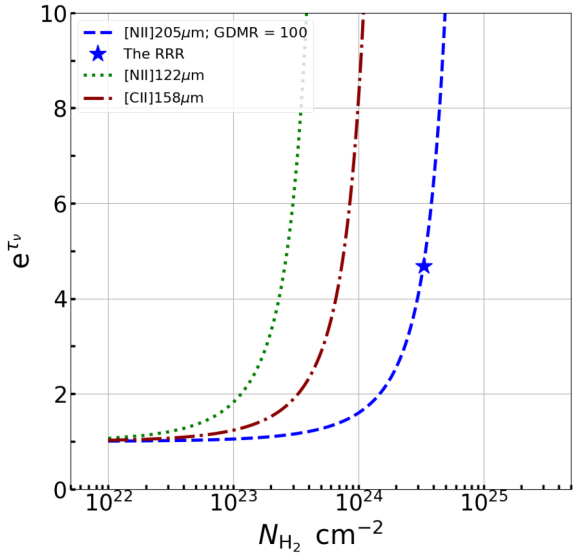

Figure 4. The dust attenuation correction as a function of mean molecular hydrogen column density. A single uniform dust screen approximation (with GDMR = 100; dust-emissivity spectral index, $\beta = 2.03$), evaluated at: the rest wavelengths of the [N II] 205 (green dotted line), the [N II] 122 (blue dashed line), and [C II]158 μm (red dash–dotted line) line emission, including the result for the *RRR* (blue star).

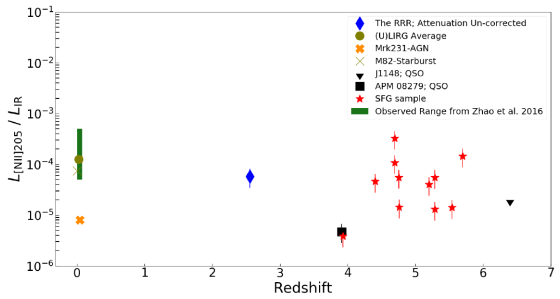

Figure 5. [N II] 205 μm line luminosity to total IR (8–1000 μm) luminosity ratio in various samples, probing a broad redshift range: local starburst, M82 (green 'x') and AGN, Mrk231 (orange 'x'), Walter et al. (2009); Decarli et al. (2012, 2014); Combes et al. (2012); Nagao et al. (2012); Béthermin et al. (2016); Pavesi et al. (2016, 2018a); Lu et al. (2018) (red stars), including the attenuation corrected value for the *RRR*. We show the predicted dispersion observed in the local Universe by Zhao et al. (2016) within a sample of galaxies with similar FIR colour as the *RRR* (green line).

(i.e. $\log(f_{70\,\mu m}/f_{160\,\mu m}) \sim 1.35$; see fig. 3 in Zhao et al. 2016). The FIR colours can be interpreted as a proxy for the dust temperature. The ratio of the FIR FSL luminosity to IR luminosity in local ULIRGs, both with and without an AGN, reveals a so-called line-to-FIR-continuum 'deficit', where the relative cooling efficiency of the line luminosity decreases with respect to the FIR continuum. This 'deficit' increases for higher values of IR luminosity (warmer FIR colour) for [N II] 205, [N II] 122, [C II] 158, [O I] 63, and [O III] 88 μm, with a two order of magnitude scatter for the [N II] lines (Graciá-Carpio et al. 2011; Malhotra et al. 2001; Díaz-Santos et al. 2017). The nature of this deficit can strongly depend on the location of dust grains along the line of sight to the line emitting region (Díaz-Santos et al. 2013, 2017), and that the 'deficit' has a tight correlation to the relative compactness of the IR luminosity surface densities.

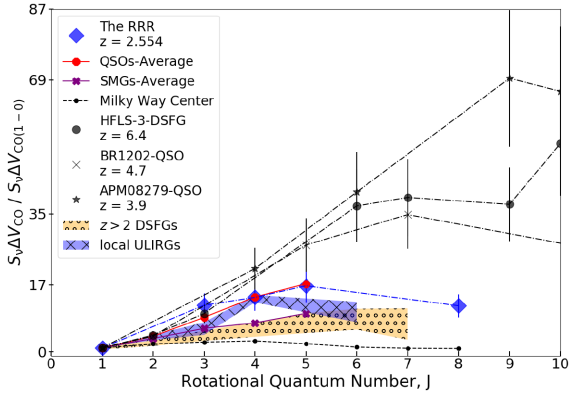

Figure 6. CO spectral line energy distribution (SLED), normalized to the ground-state CO(1-0) integrated flux density, of the *RRR* (blue diamonds), including local ULIRGs (Papadopoulos et al. 2012), the Milky Way Centre (Fixsen et al. 1999), and high-z QSOs and DSFGs (Weiß et al. 2007; Salomé et al. 2012; Bothwell et al. 2013; Riechers et al. 2013; Carilli & Walter 2013).

This reflects the spatial concentration of dust-reprocessed far-UV through IR continuum photons, which diminishes the relative cooling power of the FIR FSL. Using the maximum radius of the *RRR* in the reconstructed source plane from the best-fitting lens model of Geach et al. (2018, $R_{max} \simeq 2.6$ kpc), we infer a mean SFR surface density $\Sigma_{SFR_{IR}} = \frac{SFR_{IR}}{\pi R_{max}^2}$ of $\approx 120\,M_\odot yr^{-1}kpc^{-2}$. The high SFR surface density may indicate why the apparent, attenuated ratio of $L_{[N\,II]205\,\mu m}/L_{IR}$ has a low value compared to the mean dispersion of local SFGs with similar rest-FIR colours (see green bar in Fig. 5).

4.3 CO spectral line energy distribution

The spectral line energy distribution (SLED) of CO can be a tool to distinguish extreme, highly excited QSO galaxies from galaxies that have molecular gas excitation dominated by SF activity (Carilli & Walter 2013; Daddi et al. 2015). Fig. 6 compares the CO(1–0) normalized SLED of the *RRR* with the average spread among local ULIRGs, average DSFGs/SMGs, the Milky Way Galactic Centre, and well-known QSO powered systems at high-z (Fixsen, Bennett & Mather 1999; Weiß et al. 2007; Papadopoulos et al. 2012; Bothwell et al. 2013; Riechers et al. 2013). Compared with the Milky Way Centre and the average dusty SFG, the *RRR* shows high CO excitation. The CO SLED bears a resemblance to the even more extreme gas excitation in local ULIRGs (Papadopoulos et al. 2012; Mashian et al. 2015; Rosenberg et al. 2015), but not as high as the local starbursts, M82 (Panuzzo et al. 2010) and NGC 253 (Hailey-Dunsheath et al. 2008), or the more normal SFG, NGC 891 – all of which peak at CO(7–6) (Nikola et al. 2011). The SLED is comparable to the average value of QSOs reported in the review by Carilli & Walter (2013) out to $J_{up} = 5$. Its molecular gas excitation hints at the existence of a strong heating source. To account for the strong mid-J CO lines observed in NGC 253 and NGC 891, both Hailey-Dunsheath et al. (2008) and Nikola et al. (2011) both invoke the need for strong mechanical heating/shocks from a turbulent star-forming environment (see also Kamenetzky et al. 2016; Lu et al. 2017). The high-J turnover (at $J_{up} \geq 5$) and tail of the CO SLED indicates that the CO excitation is, however, not as extreme as in the highly excited QSO systems (Weiß et al. 2007; Salomé et al. 2012).

Table 3. The intrinsic (lensing-corrected) properties of the *RRR*.

$L_{\rm IR(8-1000\,\mu m)}$ ($10^{13}\,L_\odot$)	$L_{\rm FIR(40-120\,\mu m)}$ ($10^{13}\,L_\odot$)	$\rm SFR_{IR}$ ($M_\odot\,yr^{-1}$)	$\rm SFR_{[N\,II]205}$ ($M_\odot\,yr^{-1}$)	$M_{\rm H_2}$ ($10^{10}\,M_\odot$)	$M_{\rm min}(H^+)$ ($10^{10}\,M_\odot$)
$1.46^{0.07}_{-0.06}$	$0.82^{0.04}_{-0.03}$	2482 (992)	621	3.67 (0.9)	0.89

Note: The reported values can be converted back to the apparent values by multiplying the average lensing magnification factor of $\mu = 15$ (Geach et al. 2018). The intrinsic SFR and $M(H^+)$ are derived from the [N II] 205 μm emission line, and are corrected by factor of 4.67 to account for the derived attenuation assuming a uniform dust screen approximation. The total and FIR derived luminosities are derived from the dust SED modelling of the photometry from Harrington et al. (2016); Su et al. (2017); Rivera et al. (2018); Geach et al. (2015, 2018).

4.4 Ionized and molecular gas mass

Local [N II] measurements find that the electron density in both the Milky Way ($n_{e^-} = 33\,cm^{-3}$; Goldsmith et al. 2015) and local (U)LIRGs ($n_{e^-} = 22\,cm^{-3}$; Zhao et al. 2016) is less than $\sim 300\,cm^{-3}$. The minimum mass of ionized hydrogen can be approximated, after correcting for the line attenuation, using the high-temperature/high-density limit (see Ferkinhoff et al. 2011; Decarli et al. 2012). Using equation (1) in Decarli et al. (2012), we find $M_{\rm min}(H^+) = 0.93 \pm 0.19 \times 10^{10}\,M_\odot$. This assumes a gas-phase nitrogen abundance of, $\chi(N) = N/H = 9.3 \times 10^{-5}$ (Savage & Sembach 1996), determined by UV-absorption sightlines towards massive stars in the Milky Way. We also assume that all the nitrogen is in the singly ionized state, i.e. $\chi(N) = \chi(N^+)$. To calculate the relevant fraction of ionized to molecular gas mass, we use the measured $L'_{\rm CO(1-0)}$ line luminosity converted to a total molecular gas mass. Here we assume a CO line to molecular hydrogen gas mass conversion factor, $\alpha_{\rm CO} = 1\,M_\odot\,(K\,km\,s^{-1}\,pc^2)^{-1}$, appropriate for ULIRGs (Sanders & Mirabel 1996; Downes & Solomon 1998; Solomon & Vanden Bout 2005b),[4] and find $M_{\rm mol} = 3.67 \pm 0.9 \times 10^{10}\,M_\odot$. To account for the total molecular gas mass, we correct by the additional mass-weighted contribution by He ($1.36 \times M_{\rm H_2}$). The ionized to molecular mass fraction is 25 per cent, consistent with other actively star-forming high-z systems (Ferkinhoff et al. 2011; Zhang et al. 2018).

5 DISCUSSION

5.1 Ionized nitrogen as an SFR tracer

Despite the advantage of directly probing the ionizing stars on time-scales of ∼10 Myr, H α SFRs are often plagued by uncertainties from dust attenuation (Kennicutt 1998; Calzetti et al. 2007, 2000). In dust-obscured galaxies, the attenuation-corrected H α luminosity measurements significantly underestimate the overall SFR (e.g. Whitaker et al. 2017) derived from the total IR (8–1000 μm) luminosity (Kennicutt 1998; Kennicutt & Evans 2012). In these dust-rich galaxies, the total IR luminosity has thus been seen as the ideal tracer of SFR because the dust-absorption cross-section peaks at the wavelengths emitted by young stellar populations, and is re-emitted by dust in the far-IR wavelength regime (e.g. 40–120 μm, Helou, Soifer & Rowan-Robinson 1985). IR-derived SFRs trace the *characteristic, rather than instantaneous,* rates of SF on the order of 100 Myr, depending on the SF history. The total IR luminosity will be mostly dominated by the OB stellar population in starburst systems with less than a few 100 Myr gas consumption time-scales (Kennicutt & Evans 2012).

[4] A range has been reported for individual ULIRGs: $\alpha = 0.6$–2.6 (Downes & Solomon 1998).

The FIR FSLs have longer rest wavelengths as compared to optical or near-IR tracers of SF, and the line photons may thus escape dust-obscured H II regions without being absorbed. This motivates the use of FIR FSLs as faithful tracers of the most recent SF (Fernández-Ontiveros et al. 2016). For example, the [N II] derived SFR probes *quasi-instantaneous* SFRs corresponding to ∼30 Myr, i.e. the lifetimes of early B-stars.

Locally, however, [N II] may not be the ideal SFR tracer for galaxy integrated measurements, as it can trace a mixture of both ambient, diffuse ionized gas and ionized gas closely associated with SF. In contrast, [N II] may be a more accurate tracer of the global SFR in gas-rich SFGs at high-z, as the latter contains star-forming environments that pervade the entire ISM. Indeed, these systems undergo rapid stellar mass assembly, with SF taking place throughout the entire galaxy (Magdis et al. 2016; Rujopakarn et al. 2016; Chen et al. 2017; Elbaz et al. 2018).

As first presented in Ferkinhoff et al. (2015), there is a physically motivated relation between the SFR and [N II] line emission for SFGs. This relation is further substantiated by an empirical relation between the observed [N II] line emission and the IR-derived SFR (Zhao et al. 2016). In ionization bounded, low-density H II regions, the [N II] line emission is proportional to the ionizing photon rate (modulo the *N*/*H* ratio), which in turn is proportional to SF. The low-z relation of [N II] line luminosity to SFR can be extended out to high-z only by making strong assumptions of both the fractional nitrogen abundance and ionized gas densities (Herrera-Camus et al. 2016). Here we focus on the SFR estimate where the densities are below the critical density for [N II] 205 μm emission line (44 cm^{-3}; Goldsmith et al. 2015), and use equation (10) of Herrera-Camus et al. (2016). We assume the collisional excitation coefficients from Tayal (2011), which yields

$$\rm SFR_{[N\,II]205\,\mu m}\,[M_\odot\,yr^{-1}] = 1.98 \times 10^{-7}\,\frac{(N/H)_\odot}{(N^+/H^+)}\,\frac{L_{\rm [N\,II]205\,\mu m}}{L_\odot}. \quad (3)$$

We estimate an attenuation, and magnification corrected $\rm SFR_{[N\,II]205\,\mu m} = 621\,M_\odot\,yr^{-1}$. However, both the nitrogen abundances in the *RRR* are unknown, and will affect this measurement significantly. The [N II] 205 μm derived SFR is about 4 times smaller than the traditional IR-derived SFR (Table 3).

The SFR derived using equation (3) is, however, a lower limit. The low-density assumption breaks down when the density reaches or even exceeds that of the critical density. This is a possibility for the *RRR*, as a strong SB could result in increased electron densities and an overlap of H II regions from widespread SF, yielding electron densities $>10^4\,cm^{-3}$ (see Section 4.2.1 and theoretical [N II] line ratio versus n_{e^-} in Goldsmith et al. 2015; Herrera-Camus et al. 2016). When the electron density is significantly higher than the critical density for the ground state, the system is thermalized. Thus, the emission of photons, as defined by the Boltzmann

level population and the Einstein A-coefficient,[5] saturating the [N II] 205 μm line emission. Such high SFR surface density in the *RRR* (see Section 4.2.2) implies the ISM has an electron density $n_{e^-} >> 100$–$1000\,cm^{-3}$ (Herrera-Camus et al. 2016), i.e. an order of magnitude higher than the critical density of the [N II] 205 μm emission line. To confirm that the disagreement between these two SFR estimates is simply due to high electron density in the ISM of the *RRR*, detection of the [N II] 122 μm emission line will be needed.

5.2 Co-evolution of AGN/SF in the *RRR*

The known compact radio-mode AGN, inferred from high spatial resolution eMERLIN observations (Geach et al. 2015), does not seem to halt the intense SF activity of the *RRR* (Geach et al. 2018). The unattenuated ratio of [N II] 205 μm and IR luminosity is consistent with an SB galaxy, while the dust/CO SED also disfavours a strong AGN contaminating the IR spectrum (e.g. Weiß et al. 2007; Salomé et al. 2012). The similitude in line profile shapes of the multiple CO lines and the [N II] 205 μm line points at the co-existence of warm ionized and cold molecular phases across kpc scales.

As an example, the spatial co-existence of warm ionized regions traced by [N II] 205 μm , and that of the dense and diffuse molecular gas traced by CO, can be considered similar to the gas-phase mixing in the Central Molecular Zone (CMZ) on the scales of 100 pc (Kruijssen & Longmore 2013; Ginsburg et al. 2018), and even in the immediate vicinity of Sgr-A* on the scale of 1 pc (Moser et al. 2017). Hence, the Galactic Centre region may serve as a high-z galaxy analogue (see also Swinbank et al. 2011; Kruijssen & Longmore 2013). Thermal instability during AGN and SB phases in galaxies is one mechanism to explain how such a co-existence may be maintained over the long term. Różańska et al. (2014) and Różańska et al. (2017) found that for certain parameter ranges (activity of a galactic nucleus, star cluster input), thermal instability operates[6] and essentially leads to the formation of the two-phase (warm–cold) medium, which is rather stable given the long heating and cooling time-scales (Field 1965). This can be one of the main sources of cold gas formation under the presence of stellar, supernova, and AGN feedbacks (Tenorio-Tagle et al. 2013). Our global measurements represent the galaxy integrated average of the CO and [N II] 205 μm line emission, such that it is not possible to access the relevant physical scales to compare directly to the CMZ. Geach et al. (2015, 2018) identify a compact radio AGN (<250 pc) and a galactic disc traced by CO(4–3), extended over 2.5–3 kpc, therefore the CO(5–4) line emission is almost certainly associated with this molecular disc. However, the relative contributions of the AGN and the large-scale galactic disc to the observed [N II] 205 μm line emission remains to be resolved.

Such co-eval AGN/SF processes within galaxies is expected to be a part of the evolution of a massive galaxy such as the *RRR*, depicted by a short-lived, merger-induced SB that catalyses high AGN activity and black hole growth (e.g. Hopkins et al. 2008). There is a range of co-eval AGN/SF processes that can be seen both locally and at high-z. In local systems, nuclear regions with high SF and low-AGN fractions are observed to co-exist based on various nebular line diagnostics (e.g. D'Agostino et al. 2018), while there is an inferred quenching of SF in local AGN hosts residing in massive elliptical galaxies (Baron et al. 2018; McPartland et al. 2019). The increased excitation conditions within the narrow emission line regions of an unobscured AGN can ionize the entire ISM (Greene et al. 2011), and potentially quench SF. Therefore the use of ionized nitrogen as a tracer of SF may be unreliable because of the change in ionization structure of nitrogen (depending on the slope of the ionization parameter) in the presence of such a strong heating source. High-z galaxies, however, with large reservoirs of molecular gas ($>10^{9\text{–}10}\,M_\odot$) can sustain ongoing SF even in the most extreme, optically bright, broad-line QSO systems (Cresci et al. 2015; Glikman et al. 2015; Alaghband-Zadeh et al. 2016). A systematic study of >100 gravitationally lensed QSOs ($z \sim 1$–4), Stacey et al. (2018) found most have both SF and AGN activity. Our conclusions in Sections 4.2.2 and 4.3 suggest it is possible for both AGN and SB activity to co-exist, and this may be due to both thermal instability and the large molecular gas reservoir in the *RRR*.

6 SUMMARY AND CONCLUSIONS

We present the detection of [N II] 205 μm in a strongly lensed AGN/SB galaxy at $z = 2.5535 \pm 0.0006$, obtained using the *APEX* telescope. We complement this detection with multiple CO line transitions (CO 1–0, 5–4, 8–7) to examine the global properties of the ionized and molecular gas in the *RRR*. Our main conclusions are:

(i) The line profiles for the CO and the [N II] 205 μm emission lines have similar velocity components that can be explained by shared volumes, i.e. molecular clouds well mixed with H II regions, suggesting the majority of the strong [N II] 205 μm detection is associated with SF.

(ii) The non-negligible dust attenuation at rest-frame 205 μm in the *RRR* suggests that these corrections need to be accounted for when interpreting FIR FSLs in dust-rich systems at high-z. Assuming a uniform dust screen approximation results in a dust attenuation correction, $e^{\tau_{205\,\mu m}}$, of ∼4.67 for the *RRR*. This implies a mean H_2 gas column density $>10^{24}\,cm^{-2}$, assuming a molecular gas-to-dust mass ratio of 100.

(iii) We derived an attenuation corrected, minimum ionized gas mass, $M_{min}(H^+) = 0.89 \times 10^{10}(\frac{15}{\mu})\,M_\odot$, assuming a high-density / high-temperature limit. This ionized gas mass corresponds to about 25 per cent of the total molecular gas mass derived using the measured CO(1–0) line luminosity and $\alpha_{CO} = 1\,M_\odot$ (K km s^{-1}pc^2)$^{-1}$.

(iv) The attenuation corrected value of $L_{[N\,II]205\,\mu m}/L_{IR} = 2.7 \pm 1.0 \times 10^{-4}$, resembles the average values of SFGs rather than those with a known QSO influence.

(v) The IR SFR, $SFR_{IR} = 2482 \pm 992\,M_\odot\,yr^{-1}$, is a factor of 4 larger than the lower limit SFR estimate from the attenuation corrected, [N II] 205 μm line luminosity in the low-density regime: $SFR_{[N\,II]205} = 621\,M_\odot\,yr^{-1}$. This suggests the electron density is significantly high, or the assumed nitrogen abundance is significantly lower.

Utilizing the [N II] 205 μm line as a tracer of SF has a strong physical motivation, although the reliable application of local relations requires extensive calibration for high-z dusty SFGs. Future spatially resolved [N II] 205 and [N II] 122 μm observations would

[5] We assume all of the nitrogen is within low-density H II regions, as opposed to the hottest clusters of early O-type stars (which would result in most of the nitrogen residing in the [N III] or [NIV], rather than [N II]).

[6] S-curve in the temperature–ionization parameter plane ($T - \Sigma$), where the ionization parameter Σ is defined as $\Sigma = P_{rad}/P_{gas}$, where P_{rad} and P_{gas} are radiation and gas pressure, respectively.

help to isolate low-density versus high-density H II complexes in the warm ionized medium (as seen in Spinoglio et al. 2015; Zhao et al. 2016) in order to aid future interpretations in this system.

ACKNOWLEDGEMENTS

The authors would like to thank the referee for her/his comments and suggestions to enhance the quality of the manuscript. KCH extends his appreciation to the entire facility staff/observers/operators at the GBT, IRAM 30 m, and APEX for making the accommodation and observing welcoming and successful. The Green Bank Observatory is a facility of the National Science Foundation operated under cooperative agreement by Associated Universities, Inc. IRAM is supported by INSU/CNRS (France), MPG (Germany), and IGN (Spain). This work is carried out within the Collaborative Research Centre 956, sub-project [A1, C4], funded by the Deutsche Forschungsgemeinschaft (DFG). DR acknowledges support from the National Science Foundation under grant number AST-1614213. This publication is based on data acquired with the Atacama Pathfinder Experiment (APEX) Telescope. APEX is a collaboration between the Max-Planck-Institut fur Radioastronomie, the European Southern Observatory, and the Onsala Space Observatory. TKDL acknowledges support from the NSF through award SOSPA4-009 from the NRAO and support from the Simons Foundation. The Flatiron Institute is supported by the Simons Foundation.

REFERENCES

Alaghband-Zadeh S., Banerji M., Hewett P. C., McMahon R. G., 2016, MNRAS, 459, 999
Baldwin J. A., Phillips M. M., Terlevich R., 1981, PASP, 93, 5
Baron D. et al., 2018, MNRAS, 480, 3993
Bennett C. L. et al., 1994, ApJ, 434, 587
Bennett C. L., Larson D., Weiland J. L., Hinshaw G., 2014, ApJ, 794, 135
Béthermin M. et al., 2016, A&A, 586, L7
Bothwell M. S. et al., 2013, MNRAS, 429, 3047
Brisbin D., Ferkinhoff C., Nikola T., Parshley S., Stacey G. J., Spoon H., Hailey-Dunsheath S., Verma A., 2015, ApJ, 799, 13
Brott I. et al., 2011, A&A, 530, A115
Calzetti D., Armus L., Bohlin R. C., Kinney A. L., Koornneef J., Storchi-Bergmann T., 2000, ApJ, 533, 682
Calzetti D. et al., 2007, ApJ, 666, 870
Cañameras R. et al., 2015, A&A, 581, A105
Carilli C. L., Walter F., 2013, ARA&A, 51, 105
Casey C. M. et al., 2012, ApJ, 761, 139
Chen C.-C. et al., 2017, ApJ, 846, 108
Cicone C. et al., 2014, A&A, 562, A21
Cicone C. et al., 2015, A&A, 574, A14
Cicone C. et al., 2018, ApJ, 863, 143
Colgan S. W. J., Haas M. R., Erickson E. F., Rubin R. H., Simpson J. P., Russell R. W., 1993, ApJ, 413, 237
Combes F. et al., 2012, A&A, 538, L4
Cormier D. et al., 2015, A&A, 578, A53
Cresci G. et al., 2015, ApJ, 799, 82
Crowther P. A., 2007, ARA&A, 45, 177
D'Agostino J. J., Poetrodjojo H., Ho I. T., Groves B., Kewley L., Madore B. F., Rich J., Seibert M., 2018, MNRAS, 479, 4907
Daddi E. et al., 2015, A&A, 577, A46
Dale D. A., Helou G., Contursi A., Silbermann N. A., Kolhatkar S., 2001, ApJ, 549, 215
Dalla Vecchia C., Schaye J., 2008, MNRAS, 387, 1431
Dannerbauer H., 2019, AJ, 158, 11
Decarli R. et al., 2012, ApJ, 752, 2
Decarli R. et al., 2014, ApJ, 782, L17
Díaz-Santos T. et al., 2013, ApJ, 774, 68
Díaz-Santos T. et al., 2017, ApJ, 846, 32
Dietrich J. et al., 2018, MNRAS, 480, 3562
Downes D., Solomon P. M., 1998, ApJ, 507, 615
Ekström S. et al., 2012, A&A, 537, A146
Elbaz D. et al., 2018, A&A, 616, A110
Farrah D. et al., 2013, ApJ, 776, 38
Feltre A., Hatziminaoglou E., Fritz J., Franceschini A., 2012, MNRAS, 426, 120
Ferkinhoff C., Hailey-Dunsheath S., Nikola T., Parshley S. C., Stacey G. J., Benford D. J., Staguhn J. G., 2010, ApJ, 714, L147
Ferkinhoff C. et al., 2011, ApJ, 740, L29
Ferkinhoff C., Brisbin D., Nikola T., Stacey G. J., Sheth K., Hailey-Dunsheath S., Falgarone E., 2015, ApJ, 806, 260
Fernández-Ontiveros J. A., Spinoglio L., Pereira-Santaella M., Malkan M. A., Andreani P., Dasyra K. M., 2016, ApJS, 226, 19
Field G. B., 1965, ApJ, 142, 531
Fischer J. et al., 2010, A&A, 518, L41
Fixsen D. J., Bennett C. L., Mather J. C., 1999, ApJ, 526, 207
Frayer D. T., Maddalena R. J., Ivison R. J., Smail I., Blain A. W., Vanden Bout P., 2018, ApJ, 860, 87
Fu H. et al., 2012, ApJ, 753, 134
Geach J. E. et al., 2015, MNRAS, 452, 502
Geach J. E., Ivison R. J., Dye S., Oteo I., 2018, ApJ, 866, L12
Genzel R. et al., 2010, MNRAS, 407, 2091
Ginsburg A. et al., 2018, ApJ, 853, 171
Glikman E., Simmons B., Mailly M., Schawinski K., Urry C. M., Lacy M., 2015, ApJ, 806, 218
Goldsmith P. F., Yıldız U. A., Langer W. D., Pineda J. L., 2015, ApJ, 814, 133
Graciá-Carpio J. et al., 2011, ApJ, 728, L7
Greene J. E., Zakamska N. L., Ho L. C., Barth A. J., 2011, ApJ, 732, 9
Güsten R., Nyman L. Å., Schilke P., Menten K., Cesarsky C., Booth R., 2006, A&A, 454, L13
Hailey-Dunsheath S., Nikola T., Stacey G. J., Oberst T. E., Parshley S. C., Bradford C. M., Ade P. A. R., Tucker C. E., 2008, ApJ, 689, L109
Hailey-Dunsheath S., Nikola T., Stacey G. J., Oberst T. E., Parshley S. C., Benford D. J., Staguhn J. G., Tucker C. E., 2010, ApJ, 714, L162
Harrington K. C. et al., 2016, MNRAS, 458, 4383
Harrington K. C. et al., 2018, MNRAS, 474, 3866
Helou G., Soifer B. T., Rowan-Robinson M., 1985, ApJ, 298, L7
Herrera-Camus R. et al., 2016, ApJ, 826, 175
Heyminck S., Kasemann C., Güsten R., de Lange G., Graf U. U., 2006, A&A, 454, L21
Hickox R. C., Alexander D. M., 2018, ARA&A, 56, 625
Hopkins P. F., Hernquist L., Cox T. J., Kereš D., 2008, ApJS, 175, 356
Kamenetzky J., Rangwala N., Glenn J., Maloney P. R., Conley A., 2016, ApJ, 829, 93
Kennicutt J. R. C., 1998, ARA&A, 36, 189
Kennicutt R. C., Evans N. J., 2012, ARA&A, 50, 531
Kirkpatrick A. et al., 2017, ApJ, 849, 111
Klein B., Philipp S. D., Krämer I., Kasemann C., Güsten R., Menten K. M., 2006, A&A, 454, L29
Kruijssen J. M. D., Longmore S. N., 2013, MNRAS, 435, 2598
Lamarche C. et al., 2017, ApJ, 836, 123
Lamarche C. et al., 2018, ApJ, 867, 140
Leung T. K. D. et al., 2019a, ApJ, 871, 85
Leung T. K. D., Hayward C. C., Casey C. M., Staguhn J., Kovacs A., Dowell C. D., 2019b, ApJ, 876, 48
Lu N. et al., 2017, ApJS, 230, 1
Lu N. et al., 2018, ApJ, 864, 38
Madau P., Dickinson M., 2014, ARA&A, 52, 415
Maeder A., Meynet G., 2000, A&A, 361, 159
Magdis G. E. et al., 2016, MNRAS, 456, 4533
Magnelli B. et al., 2014, A&A, 561, A86
Maiolino R. et al., 2005, A&A, 440, L51
Maiolino R., Caselli P., Nagao T., Walmsley M., De Breuck C., Meneghetti M., 2009, A&A, 500, L1
Malhotra S. et al., 2001, ApJ, 561, 766

Marganian P., Garwood R. W., Braatz J. A., Radziwill N. M., Maddalena R. J., 2013, Astrophysics Source Code Library. record ascl:1303.019
Marrone D. P. et al., 2018, Nature, 553, 51
Marshall P. J. et al., 2016, MNRAS, 455, 1171
Mashian N. et al., 2015, ApJ, 802, 81
McKee C. F., Williams J. P., 1997, ApJ, 476, 144
McPartland C., Sanders D. B., Kewley L. J., Leslie S. K., 2019, MNRAS, 482, L129
Moser L. et al., 2017, A&A, 603, A68
Nagao T., Maiolino R., De Breuck C., Caselli P., Hatsukade B., Saigo K., 2012, A&A, 542, L34
Nayyeri H. et al., 2016, ApJ, 823, 17
Negrello M. et al., 2010, Science, 330, 800
Nikola T., Stacey G. J., Brisbin D., Ferkinhoff C., Hailey-Dunsheath S., Parshley S., Tucker C., 2011, ApJ, 742, 88
Oberst T. E. et al., 2006, ApJ, 652, L125
Oberst T. E., Parshley S. C., Nikola T., Stacey G. J., Löhr A., Lane A. P., Stark A. A., Kamenetzky J., 2011, ApJ, 739, 100
Panuzzo P. et al., 2010, A&A, 518, L37
Papadopoulos P. P., van der Werf P. P., Xilouris E. M., Isaak K. G., Gao Y., Mühle S., 2012, MNRAS, 426, 2601
Parkin T. J. et al., 2013, ApJ, 776, 65
Pavesi R. et al., 2016, ApJ, 832, 151
Pavesi R., 2018, preprint (arXiv:1812.00006)
Pavesi R. et al., 2018b, ApJ, 861, 43
Petuchowski S. J., Bennett C. L., Haas M. R., Erickson E. F., Lord S. D., Rubin R. H., Colgan S. W. J., Hollenbach D. J., 1994, ApJ, 427, L17
Planck Collaboration XXVII, 2015, A&A, 582, A30
Puls J., Vink J. S., Najarro F., 2008, A&AR, 16, 209
Rawle T. D. et al., 2014, ApJ, 783, 59
Riechers D. A. et al., 2013, Nature, 496, 329
Riechers D. A. et al., 2014, ApJ, 796, 84
Rivera J. et al., 2018, preprint (arXiv:1807.08895)
Rosdahl J., Schaye J., Dubois Y., Kimm T., Teyssier R., 2017, MNRAS, 466, 11
Rosenberg M. J. F. et al., 2015, ApJ, 801, 72
Różańska A., Czerny B., Kunneriath D., Adhikari T. P., Karas V., Mościbrodzka M., 2014, MNRAS, 445, 4385
Różańska A., Kunneriath D., Czerny B., Adhikari T. P., Karas V., 2017, MNRAS, 464, 2090
Rujopakarn W. et al., 2016, ApJ, 833, 12
Salomé P., Guélin M., Downes D., Cox P., Guilloteau S., Omont A., Gavazzi R., Neri R., 2012, A&A, 545, A57
Sanders D. B., Mirabel I. F., 1996, ARA&A, 34, 749
Savage B. D., Sembach K. R., 1996, ApJ, 470, 893
Scannapieco C. et al., 2012, MNRAS, 423, 1726
Schinnerer E. et al., 2016, ApJ, 833, 112
Schulz B. et al., 2017, preprint (arXiv:1706.00448)
Scoville N. et al., 2014, ApJ, 783, 84
Scoville N. et al., 2016, ApJ, 824, 63
Scoville N. et al., 2017, ApJ, 837, 150
Serjeant S., 2012, MNRAS, 424, 2429
Siebenmorgen R., Krügel E., Spoon H. W. W., 2004, A&A, 414, 123
Siebenmorgen R., Heymann F., Efstathiou A., 2015, A&A, 583, A120
Solomon P. M., Vanden Bout P. A., 2005a, ARA&A, 43, 677
Solomon P. M., Vanden Bout P. A., 2005b, ARA&A, 43, 677
Solomon P. M., Downes D., Radford S. J. E., Barrett J. W., 1997, ApJ, 478, 144
Spinoglio L., Pereira-Santaella M., Dasyra K. M., Calzoletti L., Malkan M. A., Tommasin S., Busquet G., 2015, ApJ, 799, 21
Stacey H. R. et al., 2018, MNRAS, 476, 5075
Stanway E. R., Eldridge J. J., 2019, A&A, 621, A105
Su T. et al., 2017, MNRAS, 464, 968
Swinbank A. M. et al., 2011, ApJ, 742, 11
Tacconi L. J. et al., 2010, Nature, 463, 781
Tacconi L. J. et al., 2018, ApJ, 853, 179
Tadaki K., 2019, ApJ, 876, 7
Tayal S. S., 2011, ApJS, 195, 12
Tenorio-Tagle G., Silich S., Martínez-González S., Muñoz-Tuñón C., Palouš J., Wünsch R., 2013, ApJ, 778, 159
Tsai C.-W. et al., 2015, ApJ, 805, 90
Uzgil B. D., Bradford C. M., Hailey-Dunsheath S., Maloney P. R., Aguirre J. E., 2016, ApJ, 832, 209
Vishwas A. et al., 2018, ApJ, 856, 174
Walter F., Weiß A., Riechers D. A., Carilli C. L., Bertoldi F., Cox P., Menten K. M., 2009, ApJ, 691, L1
Wardlow J. L. et al., 2013, ApJ, 762, 59
Weiß A., Downes D., Neri R., Walter F., Henkel C., Wilner D. J., Wagg J., Wiklind T., 2007, A&A, 467, 955
Weiß A., Kovács A., Güsten R., Menten K. M., Schuller F., Siringo G., Kreysa E., 2008, A&A, 490, 77
Whitaker K. E., Pope A., Cybulski R., Casey C. M., Popping G., Yun M. S., 2017, ApJ, 850, 208
Zanella A. et al., 2018, MNRAS, 481, 1976
Zavala J. A. et al., 2018, Nat. Astron., 2, 56
Zhang Z.-Y. et al., 2018, MNRAS, 481, 59
Zhao Y. et al., 2013, ApJ, 765, L13
Zhao Y. et al., 2016, ApJ, 819, 69

This paper has been typeset from a TEX/LATEX file prepared by the author.